

ORIGINAL ARTICLE

Open Access

Investigation of the Laser Powder Bed Fusion Process of Ti-6.5Al-3.5Mo-1.5Zr-0.3Si Alloy



Changchun Zhang^{1,2}, Tingting Liu^{1*}, Wenhe Liao¹, Huiliang Wei¹ and Ling Zhang¹

Abstract

Laser powder bed fusion (LPBF) is an advanced manufacturing technology; however, inappropriate LPBF process parameters may cause printing defects in materials. In the present work, the LPBF process of Ti-6.5Al-3.5Mo-1.5Zr-0.3Si alloy was investigated by a two-step optimization approach. Subsequently, heat transfer and liquid flow behaviors during LPBF were simulated by a well-tested phenomenological model, and the defect formation mechanisms in the as-fabricated alloy were discussed. The optimized process parameters for LPBF were detected as laser power changed from 195 W to 210 W, with scanning speed of 1250 mm/s. The LPBF process was divided into a laser irradiation stage, a spreading flow stage, and a solidification stage. The morphologies and defects of deposited tracks were affected by liquid flow behavior caused by rapid cooling rates. The findings of this research can provide valuable support for printing defect-free metal components.

Keywords Laser powder bed fusion, Ti-6.5Al-3.5Mo-1.5Zr-0.3Si alloy, Process parameters, Heat transfer and liquid flow, Defects

1 Introduction

Laser powder bed fusion (LPBF) uses a high-energy laser to manufacture near-net-shaped components layer by layer [1]. Ti-6.5Al-3.5Mo-1.5Zr-0.3Si is an $\alpha+\beta$ -type heat-resisting titanium alloy, and it is widely used to fabricate aircraft components [2, 3]. However, the LPBF process of Ti-6.5Al-3.5Mo-1.5Zr-0.3Si alloy is rarely reported. Furthermore, the formation of numerous defects in Ti-6.5Al-3.5Mo-1.5Zr-0.3Si alloy under inappropriate LPBF process parameters leads to a high melting point and low thermal conductivity.

Deposited tracks act as fundamental building units, and greatly influence the final product quality [4]. LPBF process parameters play an important role in deposited track formation. Under insufficient laser energy

input, balling, irregular pores, and discontinuous tracks occur in LPBF tracks [5–7]. When the laser energy input becomes excessive, LPBF tracks suffer from near-spherical pores and irregular tracks [8, 9]. Hence, it is crucial to establish a relationship between process parameters and forming quality under single-track process tests. Gong et al. [10] and Wang et al. [11] optimized the LPBF process windows of Ti6Al4V alloy. Yang et al. [12] optimized the process parameters of AlSi10Mg alloy. The influences of laser power and scanning speed on surface roughness, dimensional accuracy, and pore shape were also revealed in the aforementioned works; however, the explanations of defect formation mechanisms were different.

In recent years, charge-coupled devices (CCDs), two-color pyrometers, and high-speed cameras have been used to monitor LPBF processes online. A strong relationship exists between molten pool size and LPBF process parameters [13]. Once metal powder becomes melted by laser irradiation, the surplus input energy melts the powder around deposited tracks through heat transfer [14] and forms a denuded area around the molten pool [15]. In addition, a competition between

*Correspondence:

Tingting Liu
liutingting@mail.njust.edu.cn

¹ School of Mechanical Engineering, Nanjing University of Science and Technology, Nanjing 210094, China

² School of Mechanical and Vehicle Engineering, West Anhui University, Luan 237012, China

outward metal vapor flux and the entrainment of powder particles in a shear flow driven by a metal vapor jet exists during LPBF [16, 17]. However, a series of complex physical processes such as phase transition, heat transfer, and mass transfer, take place during LPBF in a short period. The melting liquid is generally driven by recoil pressure, surface tension, the Marangoni force, gravity, and buoyancy to form a complex flow [18, 19]. Therefore, it is necessary to accurately simulate the aforementioned phenomena to explain the microscopic and macroscopic mechanisms of LPBF. Khairallah et al. [20] established a three-dimensional (3D) high-fidelity powder-scale model and found that a depression shape and spatter defects were produced by the recoil pressure. Zhang et al. [21] observed a high-speed backward flow of $4\text{--}5\text{ ms}^{-1}$ from the beginning to the end of the molten pool. Tang et al. [22] asserted that recoil pressure and surface tension played important roles in the formation of two types of pores. Wei et al. [19] built a multi-physical field simulation model in the open-source CFD and OpenFOAM software and highlighted the effects of recoil pressure and surface tension on the LPBF tracks. However, the influences of heat transfer and liquid flow on defect formation during LPBF are not clearly stated in the above-mentioned investigations.

In the present work, the LPBF process of Ti-6.5Al-3.5Mo-1.5Zr-0.3Si alloy was optimized. A well-tested phenomenological model was used to compute heat transfer and liquid flow behaviors during LPBF, and the influences of LPBF process parameters on printing

defects were systematically described. Cooling rates were calculated accurately to assess their influences on macroscopic and microscopic alloy morphologies. The findings of this research can provide valuable support for printing defect-free metal components.

2 Methodologies

2.1 Experimental Conditions

The chemical composition of the alloy is presented in Table 1. The morphology and size distribution of spherical gas-atomized powder particles are displayed in Figure 1.

Forty-five LPBF tracks with a length of 1.5 mm were formed by a Concept Laser M2 system (Germany) by changing the laser power (P) changed from 150 W to 270 W, and the scanning speed (v) changed from 850 mm/s to 1650 mm/s. The powder layer thickness was 30 μm .

The sizes of LPBF tracks were measured by a VK-100X laser microscope (Keyence, Japan), and their surface and cross-sectional morphologies were detected by an FEI Quanta 250 F scanning electron microscope (FEI, America).

2.2 Simulation Model

The conservation equations of energy, momentum, and mass were solved concurrently using the VOF equation in OpenFOAM [23]. The details of the simulation model are available in Ref. [19]. The thermophysical properties of the alloy and Ar were calculated by JMatPro software and Ref. [24], as shown in Table 2.

Table 1 Chemical composition of the alloy (wt.%)

Ti	Al	Mo	Zr	Si	Fe	C	O	N
Bal	6.6	3.2	1.7	0.3	0.08	0.02	0.12	0.006

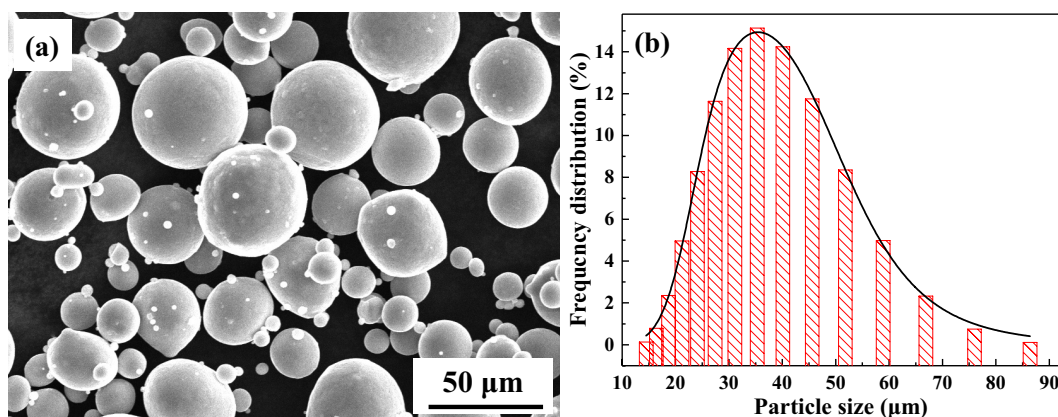


Figure 1 a Morphology and b size distribution of Ti-6.5Al-3.5Mo-1.5Zr-0.3Si powder particles

Table 2 Thermophysical properties of the alloy and Ar

Parameters	Value
Metal density ($\text{kg}\cdot\text{m}^{-3}$)	4480
Solidus temperature (K)	1844
Liquidus temperature (K)	1968
Evaporation temperature (K)	3494
β -Tranus (K)	1288
The viscosity of liquid metal ($\text{Pa}\cdot\text{s}$)	4×10^{-3}
Temperature coefficient of surface tension ($\text{N}\cdot\text{m}^{-1}\cdot\text{K}^{-1}$)	-2.6×10^{-4}
Latent heat of evaporation ($\text{J}\cdot\text{kg}^{-1}$)	9.8×10^6
Latent heat of fusion ($\text{J}\cdot\text{kg}^{-1}$)	2.86×10^5
Gas constant ($\text{J}\cdot\text{kg}^{-1}\cdot\text{mol}^{-1}$)	8.314
Stefan-Boltzmann ($\text{W}\cdot\text{m}^{-2}\cdot\text{K}^{-4}$)	5.67×10^{-8}
Thermal conductivity of Ar ($\text{W}\cdot\text{m}^{-1}\cdot\text{K}^{-1}$)	1.772×10^{-2}
Viscosity of Ar ($\text{Pa}\cdot\text{s}$)	2.2×10^{-5}
Specific heat of Ar ($\text{J}\cdot\text{kg}^{-1}\cdot\text{K}^{-1}$)	521.75

3 Results

3.1 Experimental Results

3.1.1 Optimization of Process Parameters

Discontinuous tracks [25] were formed at low laser powers (Figure 2a). With the increase of laser power, continuous tracks appeared (Figure 2b). Irregular tracks [26]

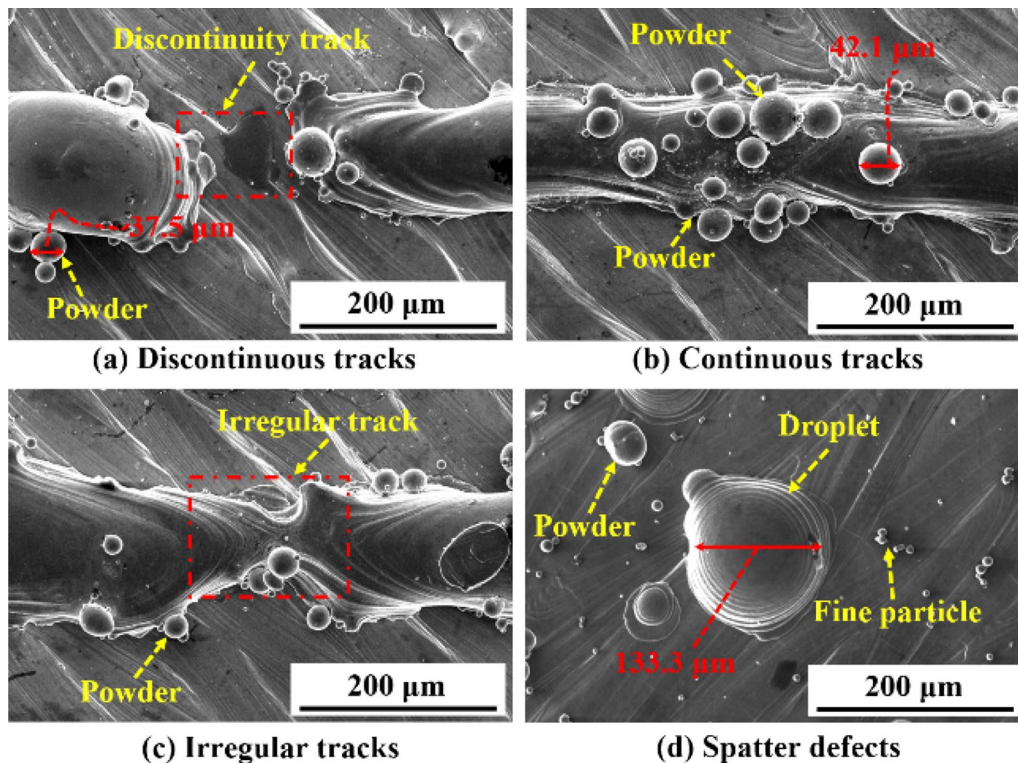
were observed when the laser power was extensively high (Figure 2c). Powder particles adhered to the surface of all deposited samples. Moreover, spatter defects [27], such as droplets and fine particles, appeared at high laser powers (Figure 2d).

The LPBF process window of Ti-6.5Al-3.5Mo-1.5Zr-0.3Si alloy is presented in Figure 3. When P was raised from 150 W to 270 W, discontinuous tracks and irregular tracks appeared, respectively. A less fine morphology was observed at $v = 1650$ mm/s. Therefore, the LPBF process window of the alloy was mainly determined at P changed from 165 W to 255 W, with v changed from 850 mm/s to 1450 mm/s.

The height fluctuation of deposited tracks was measured by VK-H1XMC software (Figure 4a), and the standard deviation value ($STDEV$) was calculated using Eq. (1). The surface roughness of the substrate was taken as the evaluation metric ($Ra \approx 12.5 \mu\text{m}$ after milling). The greater the number of samples with $STDEV < 12.5 \mu\text{m}$, the better the process parameters.

$$STDEV = \sqrt{\frac{1}{N-1} \cdot \sum_{i=1}^n (X_i - \bar{X})^2}, \quad (1)$$

where \bar{X} is the mean value of X_1, X_2, \dots, X_n .

**Figure 2** Typical morphologies of LPBF tracks

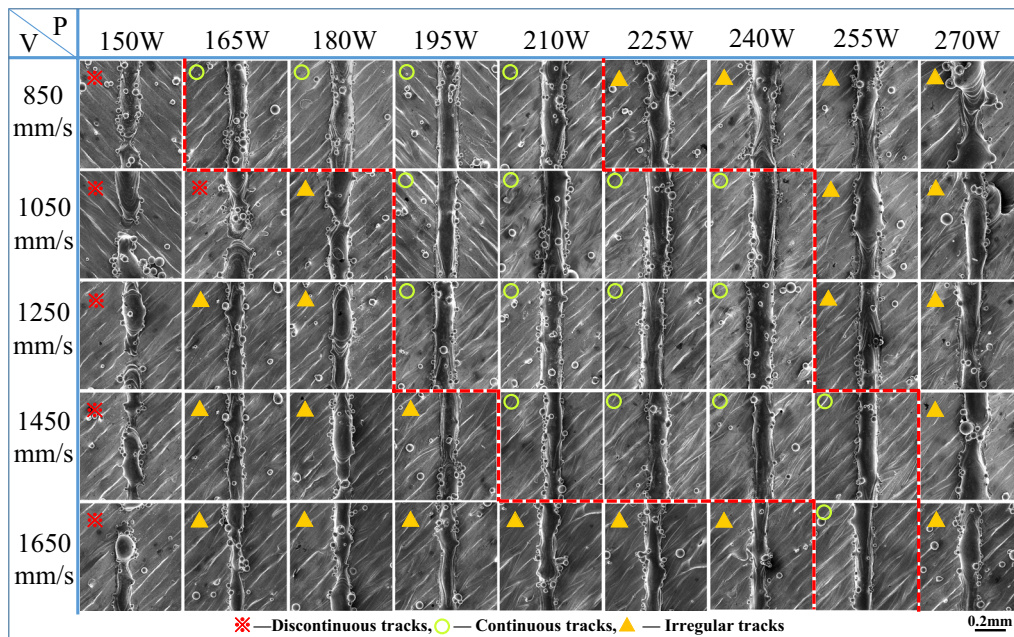


Figure 3 LPBF process window of Ti-6.5Al-3.5Mo-1.5Zr-0.3Si alloy

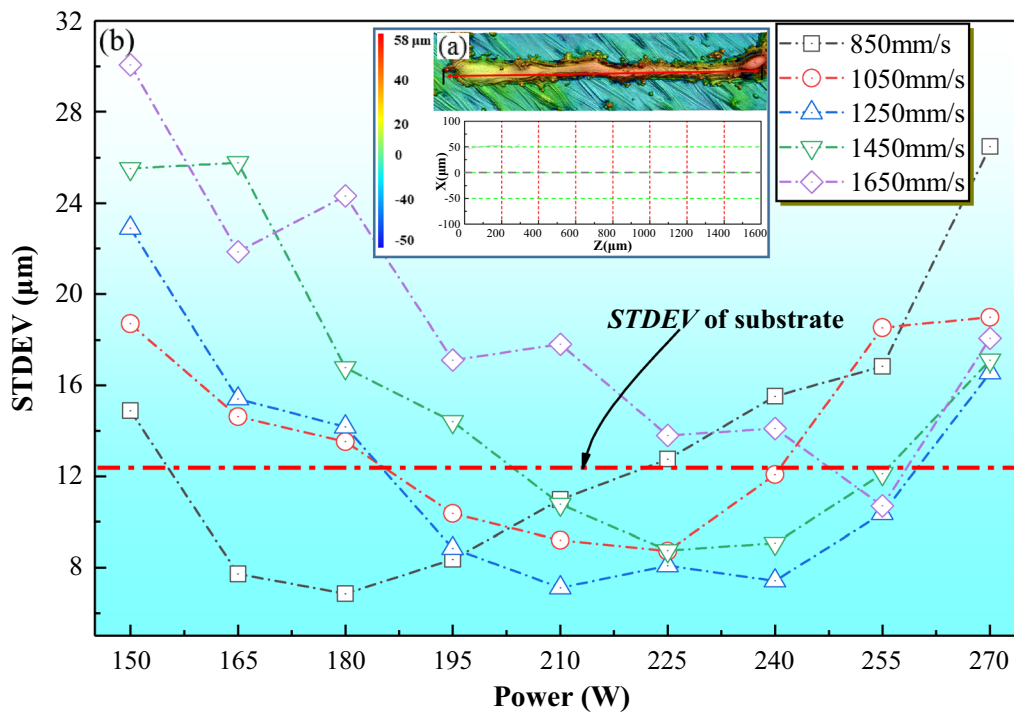


Figure 4 **a** Data measurement method, and **b** Variation of STDEVs with laser power

When P was equal to 195 W, 210 W, and 225 W, the numbers of samples (with $STDEV < 12.5 \mu\text{m}$) were 3, 4, and 3, respectively. And when v was equal to 1250 mm/s, the number of samples was 5 (Figure 4b). Therefore,

it can be inferred that LPBF tracks were excellent at P changed from 195 W to 225 W, with $v = 1250 \text{ mm/s}$. In comparison to Ti6Al4V [10, 28], Ti-6.5Al-3.5Mo-1.5Zr-0.3Si alloy required higher laser power.

3.1.2 Variation of Shape Parameters with Process Parameters

Figure 5(a) presents the sizes of LPBF tracks at $v = 1250$ mm/s. As the laser power was raised from 150 W to 270 W, the depth, width, and height of the molten pool increased by about 280% (increased from 42.2 μm to 160.3 μm), 45% (increased from 102.6 μm to 149.0 μm), and 86% (increased from 29.1 μm to 53.3 μm), respectively. Figure 5(b) presents the sizes of LPBF tracks at $P = 195$ W. As the scanning speed was raised from 850 mm/s to 1650 mm/s, the depth and width of the molten pool decreased by about 11.9% (decreased from 84.2 μm to 74.2 μm) and 25.9% (decreased from 140.2 μm to 103.9 μm), respectively, whereas the height of the molten pool first decreased and then increased. Laser power had a great influence on the depth and morphology of the molten pool, and scanning speed mainly affected the width of the molten pool.

Figure 6 exhibits the cross-sectional of LPBF tracks at $v = 1250$ mm/s. When the laser power was in the range of 150–180 W, the input energy could not completely melt the powder at the edge of the laser scanning line. Moreover, the melt viscosity was large, and the pool spreading capacity was insufficient; therefore, the cross-section of the melt after solidification was small. When the laser power was between 195 W and 225 W, the melting amount of the metal powder increased and the melt viscosity decreased; thus, the molten pool easily spread to the two sides of the laser scanning line, the cross-section of LPBF tracks became larger, and the morphology of LPBF tracks was excellent. When the laser power ranged between 240 W and 270 W, the input energy was large

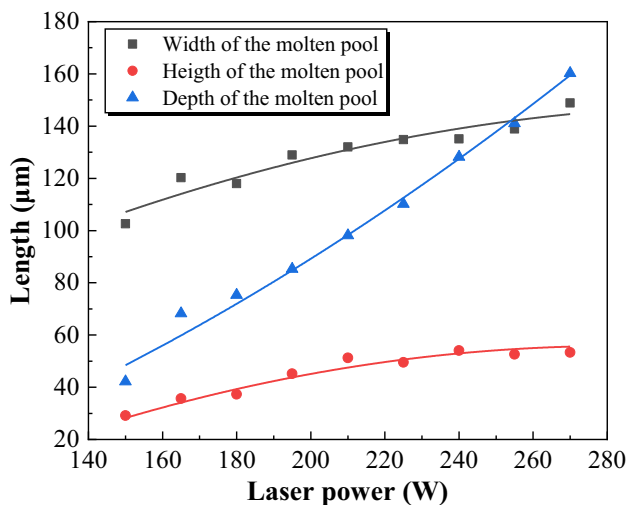
and a deep molten pool was easily produced in the laser irradiation region. In addition, some metal powder particles were vaporized instantaneously, and the molten pool was susceptible to a disturbance under the impact of the metallic vapor. Therefore, LPBF tracks had a large depth and an irregular morphology.

3.2 Simulation Results

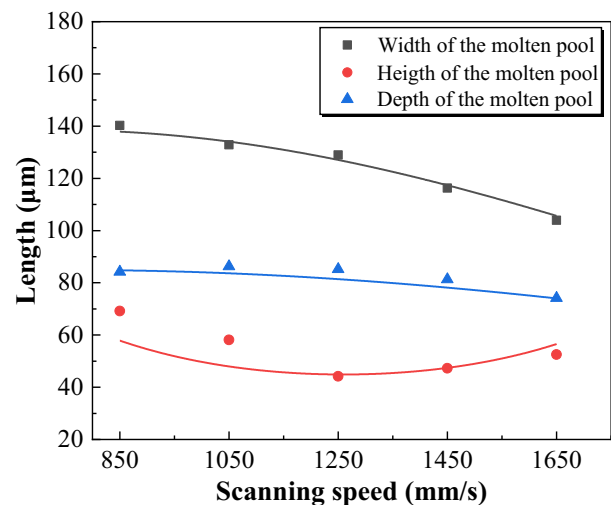
3.2.1 Molten Pool Formation

The simulation results of LPBF tracks for P were 150 W, 195 W, and 255 W, with $v = 1250$ mm/s are depicted in Figure 7. The start time, middle time, and end time of the laser operations were $t = 20$ μs , $t = 320$ μs , and $t = 580$ μs , respectively. The molten pool was defined as the region with a temperature greater than $T = 1968$ K (the liquidus temperature of Ti-6.5Al-3.5Mo-1.5Zr-0.3Si alloy (Table 2)). The highest temperature was detected at the laser spot, and the heat-affected zone (HAZ) increased with the rise of laser power. The liquid flowed from the laser spot to both sides of the molten pool. Moreover, the flow velocity near the laser spot was larger and increased with the rise of laser power (Figure 8); however, the flow direction did not vary significantly. In addition, non-melted particles on the edge of LPBF tracks had a saw tooth-like morphology (Figure 7c, f, and i), indicating that it is necessary to set a reasonable hatch distance during single-layer forming.

The variation of melt volume with time is illustrated in Figure 9a. The starting times for molten pool stabilization in the 150 W, 195 W, and 255 W samples were 80 μs , 200 μs , and 240 μs , respectively. In the stable state, the melt volume of the 150 W, 195 W, and 255 W samples were



(a) LPBF track sizes at $v = 1250$ mm/s



(b) LPBF track sizes at $P = 195$ W

Figure 5 Sizes of LPBF tracks

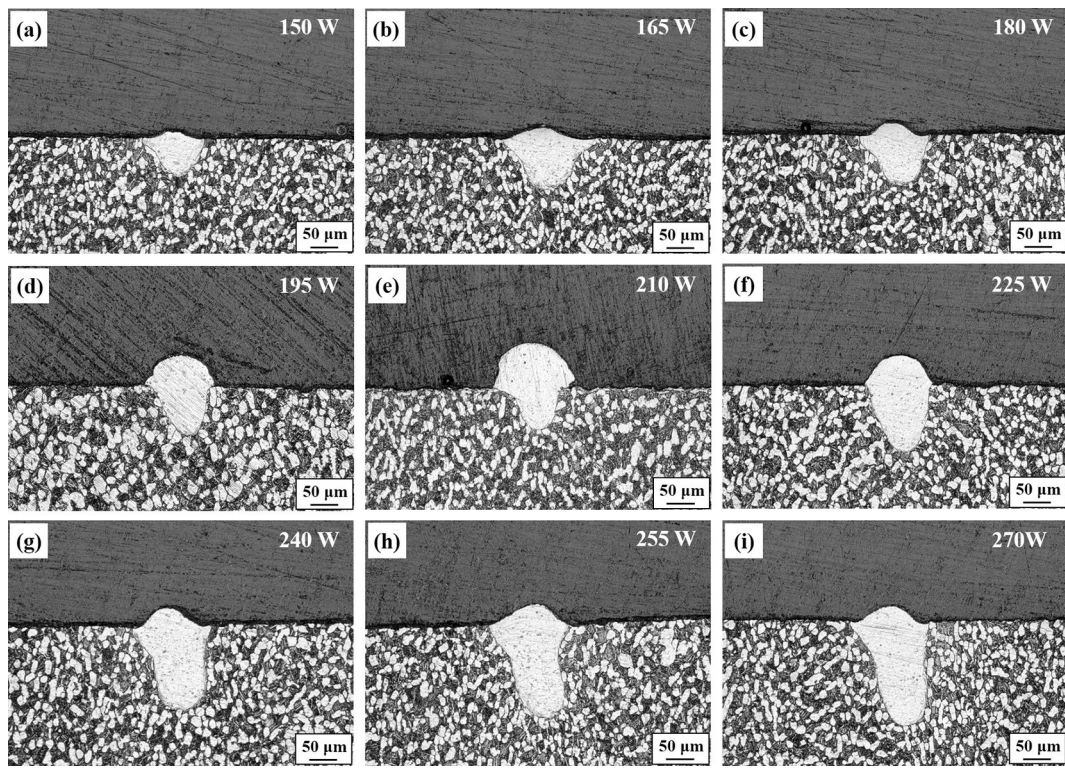


Figure 6 Cross-sectional of LPBF tracks at $v = 1250$ mm/s

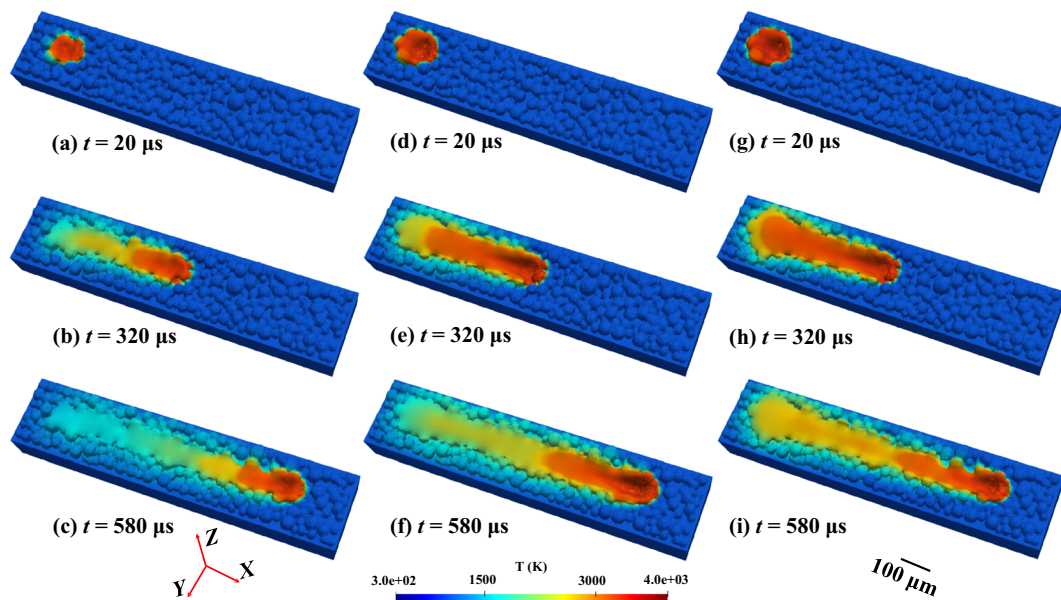


Figure 7 Simulation results of LPBF tracks: **a–c** 150 W, **d–f** 195 W, **g–i** 255 W

$1.14 \times 10^5 \mu\text{m}^3$, $5.16 \times 10^5 \mu\text{m}^3$, and $11.76 \times 10^5 \mu\text{m}^3$, respectively, and the corresponding $STDEV$ of the melt volumes were $0.11 \mu\text{m}^3$, $0.08 \mu\text{m}^3$, and $0.38 \mu\text{m}^3$, respectively, indicating that the melt volume fluctuated with

the variation of laser power in the stable state. Hence, insufficient molten pool expansion occurred in the 150 W sample, and a disturbance of the molten pool, such as Rayleigh instability occurred in the 255 W sample. The

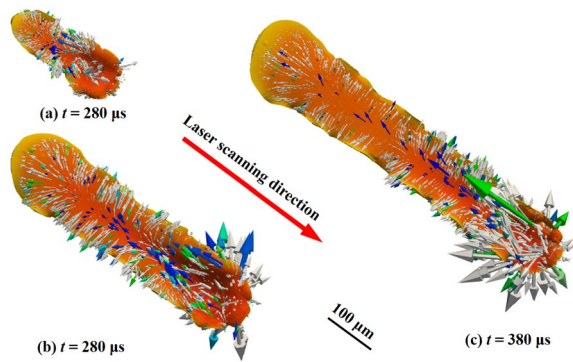


Figure 8 Liquid metal flow fields of the molten pool in the stable state: **a** 150 W, **b** 195 W, and **c** 255 W

simulation and experimental data of the molten pool dimension in the stable state are compared in Figure 9b. The error range for the molten pool dimension was 4.7%–13.6%. Therefore, it can be inferred that laser power had a greater effect on flow velocity than on flow direction. Moreover, high laser power created a large molten pool and irregular tracks.

3.2.2 Longitudinal Section of LPBF Tracks

Figure 10 shows the serial longitudinal sections of the 195 W sample. The longitudinal section position is presented in Figure 10a. The reflow liquid (flow direction differed from the laser scanning direction) was found

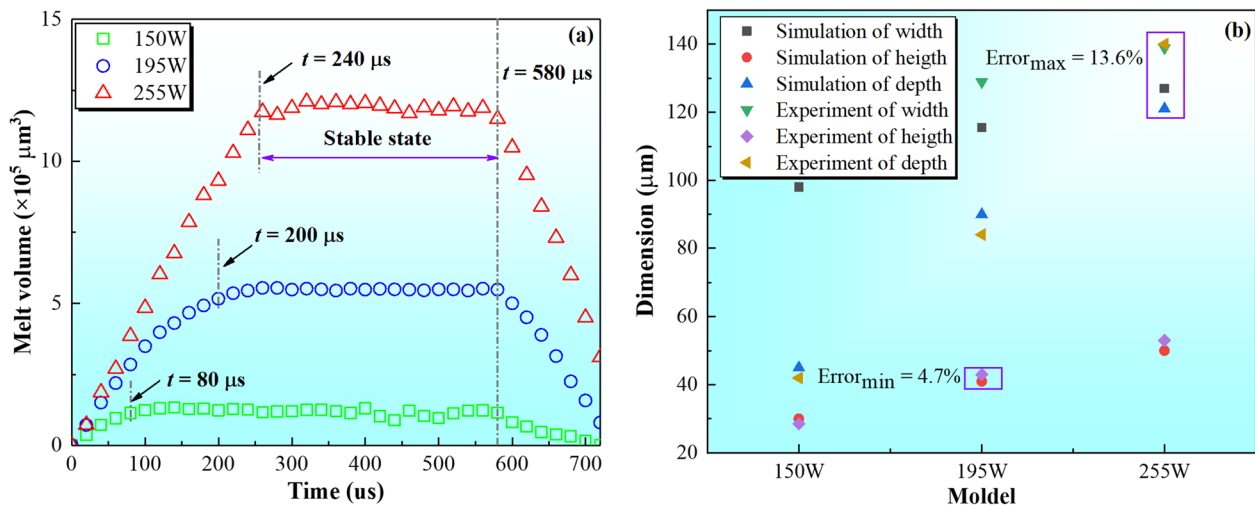


Figure 9 **a** Variation of melt volume with time and **b** The maximum molten pool dimensions in the stable state

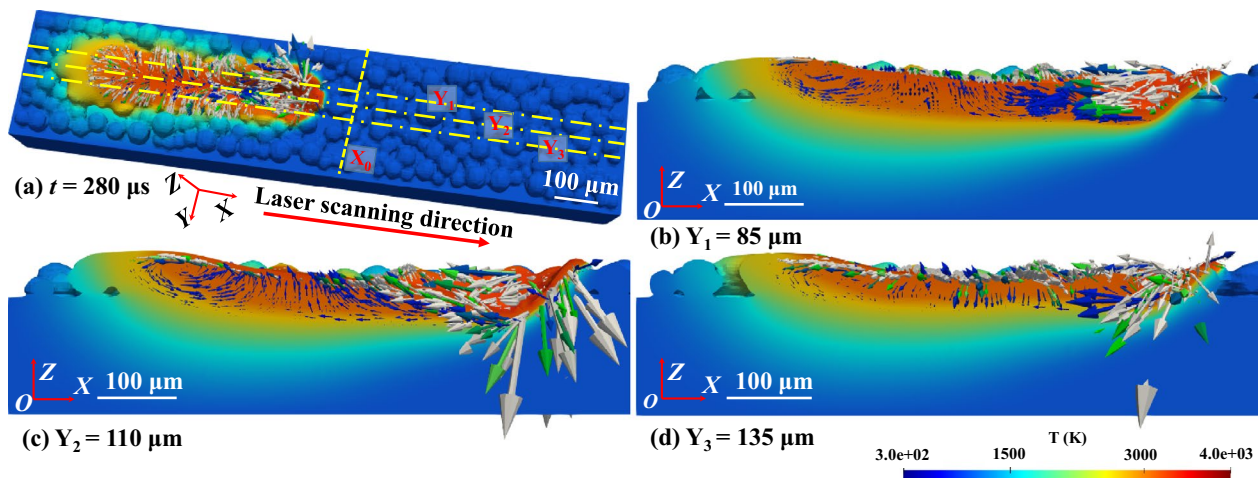


Figure 10 Serial longitudinal sections of LPBF tracks at 195 W

near the laser spot. The flow velocity in the middle of the molten pool was greater than those on both sides of the molten pool (Figure 10b–d). Moreover, a complex circular fluid appeared at the molten pool tail (Figure 10b and c), which could be attributed to the Marangoni flow driven by the surface tension gradient.

3.2.3 Longitudinal Section of LPBF Tracks

The serial cross-sections of LPBF tracks at different times are displayed in Figures 11, 12, 13. The cross-section position is presented in Figure 10a. The LPBF process could be divided into a laser irradiation stage (Figures 11a–c, 12a–c, and 13a–c), a spreading flow stage (Figures 11d–f, 12d–f, and 13d–f), and a solidification stage (Figures 11g, h, 12g, h, 13g, and h).

In the laser irradiation stage, the liquid was driven by the recoil pressure and created a depression shape. In the spreading flow stage, the molten pool temperature decreased to the melting point, and the depression shape was gradually repaired. The duration of this stage increased with the rise of laser power. The duration of this stage in the 150 W, 195 W, and 255 W samples was 80 μ s, 160 μ s, and 280 μ s, respectively. In the solidification stage, the molten pool temperature reached the ambient temperature.

The reflow liquid was found in the early spreading flow stage (Figures 11d, 12d, and 13d), and then it flowed

from the bottom to the top (Figures 11e, 12e, and 13e) and also from the center to both sides of the molten pool (Figures 11f, 12f, and 13f). The flow direction remained unchanged with the rise of laser power. The reflow had an important effect on the liquid flow and expanded the molten pool.

The thermal monitored at the cross-sections of LPBF tracks under different laser powers are shown in Figure 14. The cooling rate varied in different cooling stages. In the spreading flow stage, the cooling rates of the 150 W, 195 W, and 255 W samples were 1.67×10^7 K/s, 1.17×10^7 K/s, and 0.91×10^7 K/s, respectively, and in the solidification stage, the values were 6.93×10^6 K/s, 3.44×10^6 K/s, and 2.91×10^6 K/s, respectively. These results indicate that the liquid flow behaviors and the β -phase transformation were affected by the rapid cooling rates, resulting in the different morphologies and microstructures of LPBF tracks, respectively.

4 Discussion

4.1 Formation of LPBF Defects

A schematic illustration of the molten pool formed during LPBF is presented in Figure 15. In the laser irradiation stage, the internal energy of the alloy increased rapidly due to laser heat conduction (Figure 15b). In this experiment, the laser beam was in the TEM00 mode. The

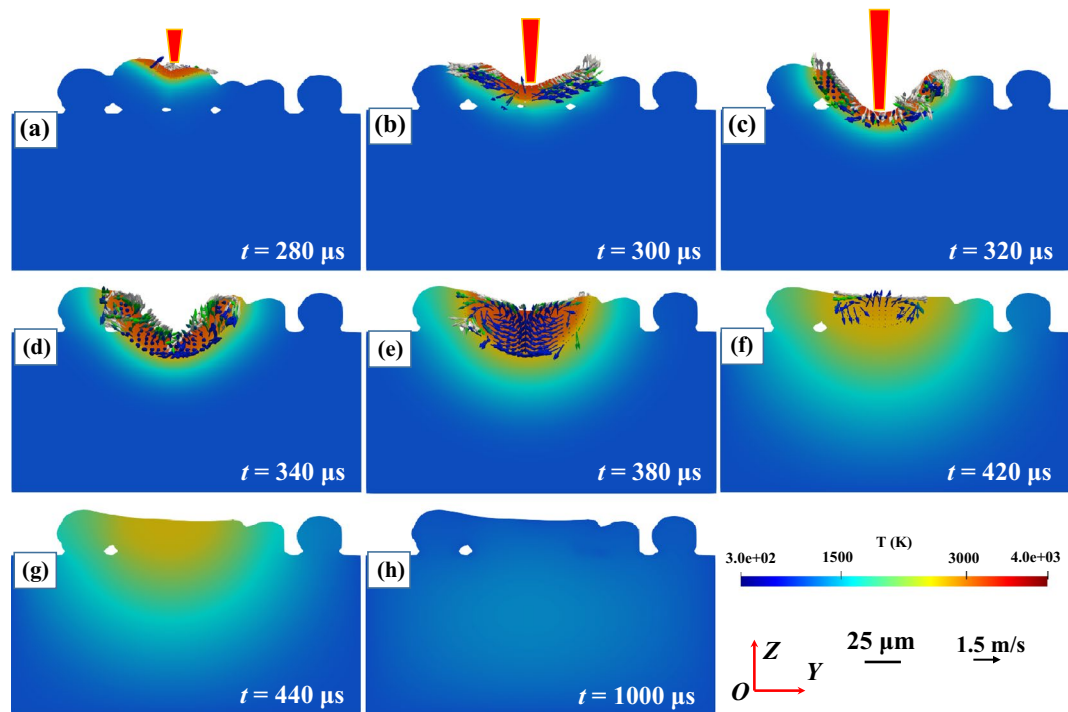


Figure 11 Serial cross-sections of LPBF tracks at 150 W

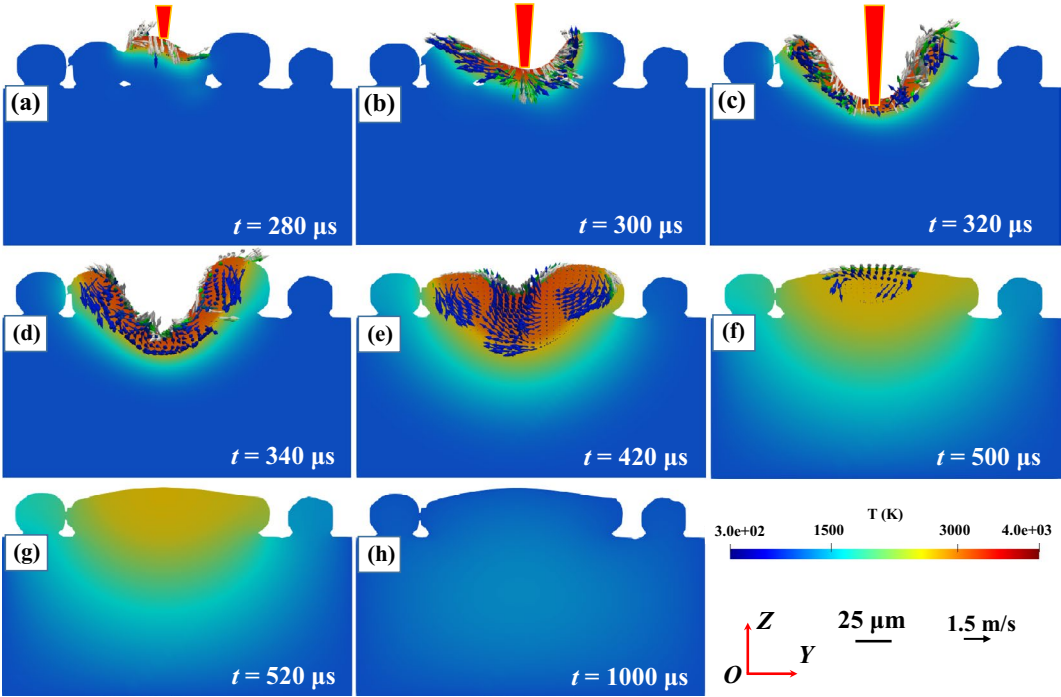


Figure 12 Serial cross-sections of LPBF tracks at 195 W

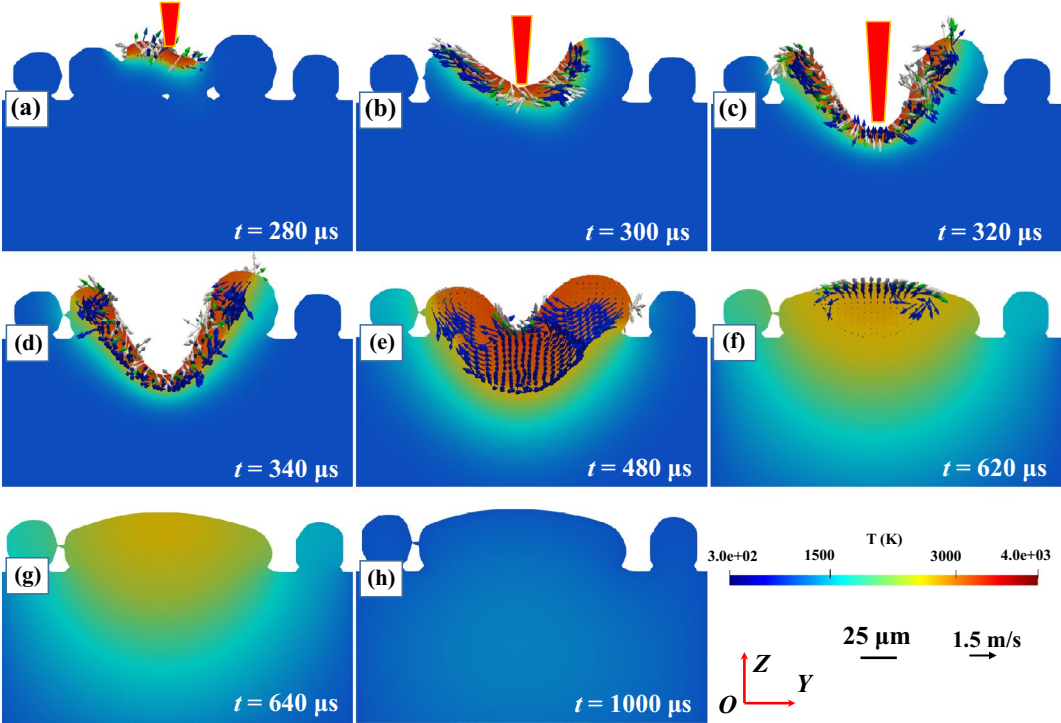


Figure 13 Serial cross-sections of LPBF tracks at 225 W

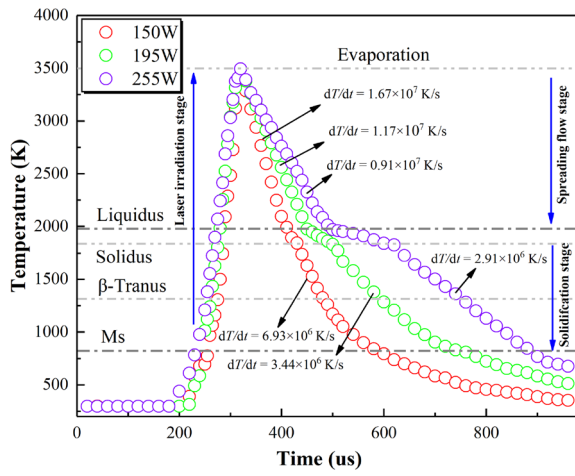


Figure 14 Thermal monitored at the cross-sections of LPBF tracks under different laser powers,

maximum temperature of the laser beam was calculated as [29].

$$T_{max} = \frac{\sqrt{2}AId}{k\sqrt{\pi}} \arctan \frac{\sqrt{2Dt_1}}{d}, \quad (2)$$

where I is determined by the laser power, D denotes the heat diffusion coefficient of the molten pool, t_1 is the interaction time between the laser and the powder, A is the material absorption rate, k is the thermal

conductivity, and d is the laser spot diameter. Therefore, the T_{max} increases with the rise of laser power.

The melt was affected by the surface tension when T_{max} reached the melting point of Ti-6.5Al-3.5Mo-1.5Zr-0.3Si alloy. When the laser power was low, the surface tension between the solid and the vapor (σ_{SV}) was also low; thus, the surface tension between the solid and the liquid (σ_{SL}) was high. According to Zhou et al. [25], Young's equation can be expressed as:

$$\cos \theta = \frac{\sigma_{SV} - \sigma_{SL}}{\sigma_{LV}}, \quad (3)$$

It is evident from Eq. (3) that balling and discontinuous tracks were prone to occur when $\theta > 90^\circ$ (Figure 2a).

When T_{max} reached the boiling point of Ti-6.5Al-3.5Mo-1.5Zr-0.3Si alloy, a positive pressure air mass on the molten pool surface produced a recoil pressure to form a depression shape. When the laser power reached the threshold value of the "keyhole" [30], spatter defects and a strong reflow liquid were formed successively.

Bidare et al. [31] found that the powder at the head of the molten pool was driven by the positive pressure air mass. Kaplan [32] clarified that a negative pressure area was formed by the positive pressure air mass quickly moving away on the molten pool surface. The Bernoulli equation can be expressed as:

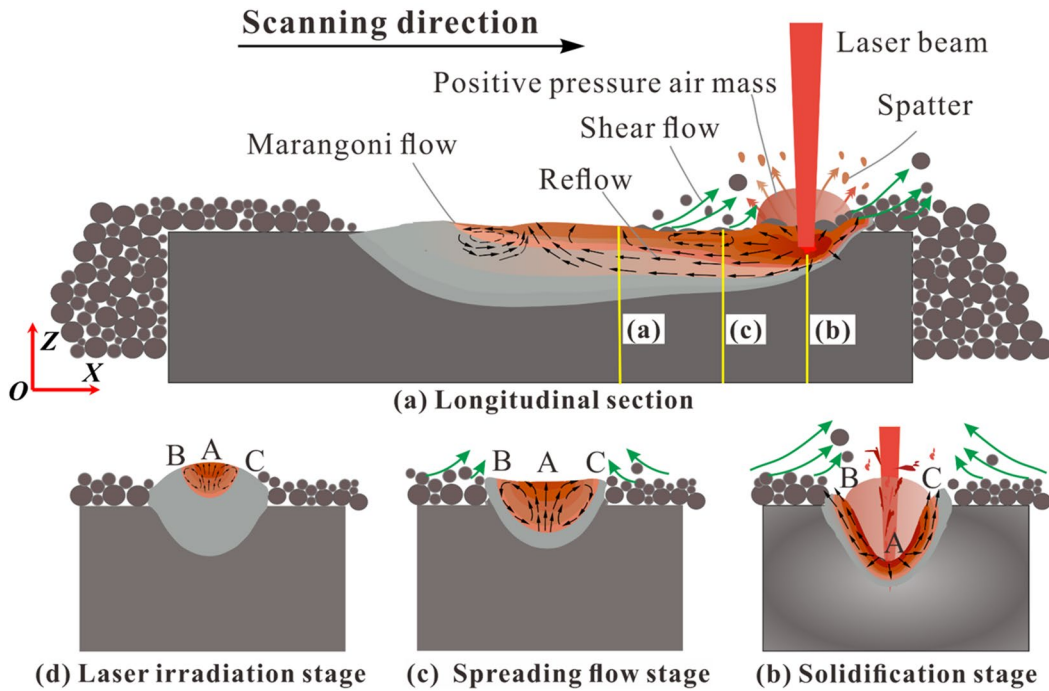


Figure 15 Schematic illustration of the molten pool formed during LPBF process

$$P_n + \frac{1}{2}\rho v^2 + \rho gh = C, \quad (4)$$

where h is the height of the test point, ρ is the density of the positive pressure air mass, P_n is the pressure of the negative pressure zone, v is the velocity of the positive pressure air mass (scanning speed), and C is a constant. The P_n decreases with the increase of v , causing an inward shear flow [31].

Matthews et al. [16] found that the powder around LPBF tracks was entrained by the shear flow and moved toward the molten pool and also numerous non-melted powder particles adhered to the surface of LPBF tracks. Laser power was mainly concentrated in the irradiation stage to affect the morphology of LPBF tracks.

In the spreading flow stage, the depression shape was gradually repaired by the reflow liquid, and the surrounding powder was dragged to the molten pool (Figure 15c). The expansion rate of the molten pool was hindered by its dynamic viscosity (μ).

$$\mu = \frac{16}{15} \sqrt{\frac{m}{k_B T}} \gamma, \quad (5)$$

where m is the atomic mass of powder particles, k_B is the Boltzmann constant, T is the liquid phase temperature, and γ is the liquid surface tension. The value of μ decreased as laser power increased. As the viscosity of the melt decreased, it spread more easily to form a large molten pool. Furthermore, a sharp surface tension gradient was induced when the laser heat input was high, leading to a Marangoni flow [33]. When the molten pool volume increased to a certain extent (length (L): width (W) > 2.1 [34]), a Rayleigh instability phenomenon occurred, and irregular tracks were formed (Figure 16).

4.2 Microstructure Formation

In the solidification stage, LPBF tracks remained fixed (Figure 15d); however, they experienced a phase transformation. The typical EBSD images of LPBF tracks are displayed in Figure 17. The strip α' phase grew along the building direction, and the metastable structures were found in the interior of the strip α' phase. The geometrical necessary dislocation (GND) density was $8.18 \times 10^{14} \text{ m}^{-2}$ which was caused by the cooling rate. The β -phase transformation was affected by the cooling rate: $\beta \rightarrow \alpha + \alpha'$ at 25–410 °C/s, and $\beta \rightarrow \alpha'$ at >410 °C/s [35]. As the LPBF cooling rate ranged from $2.91 \times 10^6 \text{ K/s}$ to $6.93 \times 10^6 \text{ K/s}$

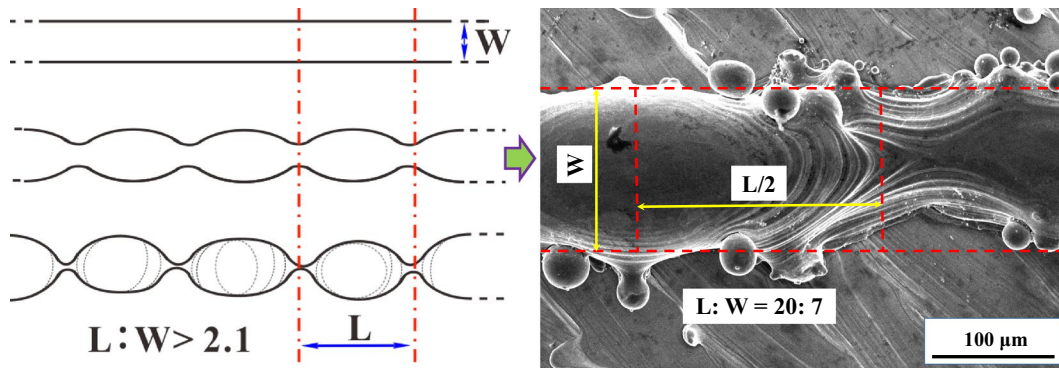


Figure 16 Rayleigh instability morphology of deposited tracks

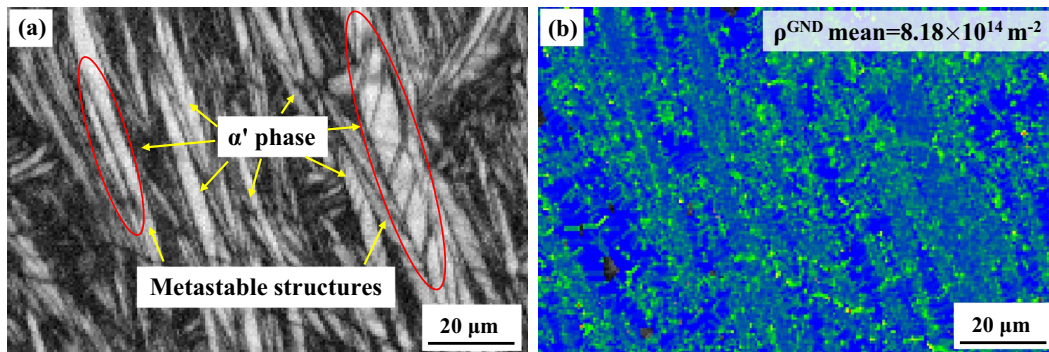


Figure 17 Typical EBSD image of LPBF track: **a** BC map, **b** GND density

in the solidification stage, it was difficult to control the β -phase transformation by laser power. However, high residual stresses were caused by the rapid cooling rates, resulting in the α' phase with metastable structures. The effects of residual stress on microstructures can be found in detail in Ref. [36].

Moreover, the LPBF process was complicated by the material characteristics of Ti-6.5Al-3.5Mo-1.5Zr-0.3Si alloy. For example, powder particles adhered around the molten pool were difficult to melt because of their high melting point, and the liquid flow time was extended because of its low thermal conductivity. Therefore, the influences of alloying elements and cooling rate on the microstructure of Ti-6.5Al-3.5Mo-1.5Zr-0.3Si alloy in the solidification stage should be explored in detail.

5 Conclusions

- (1) Discontinuous tracks, irregular tracks, and spatter defects appeared under inappropriate LPBF process parameters. LPBF tracks were excellent at P changed from 195 W to 225 W, with $v = 1250$ mm/s. Laser power had a great influence on the depth and morphology of the molten pool, and scanning speed mainly affected the width of the molten pool.
- (2) Laser power had a greater effect on flow velocity than flow direction. A large molten pool caused a Rayleigh instability phenomenon and formed irregular tracks. A low laser power caused insufficient spreading capacity and formed discontinuous tracks. A high laser power caused the volume fluctuation of the molten pool and formed irregular tracks.
- (3) The LPBF process was divided into a laser irradiation stage, a spreading flow stage, and a solidification stage. A reflow liquid, a depression shape, and spatter defects were formed in the laser irradiation stage. The depression shape was repaired by the reflow liquid in the spreading flow stage. The macroscopic morphology of deposited tracks remained in the solidification stage.
- (4) The cooling rate varied in different cooling stages. The cooling rate ranged between 0.91×10^7 K/s and 1.67×10^7 K/s in the spreading flow stage, whereas it fluctuated between 2.91×10^6 and 6.93×10^6 K/s in the solidification stage. The liquid flow behaviors and β -phase transformation of deposited tracks caused by the rapid cooling rates.

Acknowledgements

Not applicable.

Author Contributions

CZ, TL, and WL were in charge of the whole trial; CZ and HW wrote the manuscript; LZ assisted with sampling and laboratory analyses. LZ and CZ were in charge of the FM simulation. All authors read and approved the final manuscript.

Authors' Information

Changchun Zhang, born in 1983, is currently a PhD candidate at School of Mechanical Engineering, Nanjing University of Science and Technology, China. He received his bachelor degree from Changchun University of Science and Technology, China, in 2012.

Tingting Liu, born in 1975, is a professor and a PhD candidate supervisor at School of Mechanical Engineering, Nanjing University of Science and Technology, China.

Wenhe Liao born in 1965, is a professor and a PhD candidate supervisor at School of Mechanical Engineering, Nanjing University of Science and Technology, China.

Huiliang Wei, born in 1986, is a professor and a PhD candidate supervisor at School of Mechanical Engineering, Nanjing University of Science and Technology, China.

Ling Zhang, born in 1995, is currently a master candidate at Nanjing University of Science and Technology, China.

Funding

Supported by Development of a Verification Platform for Product Design, Process, and Information Exchange Standards in Additive Manufacturing (Grant No. 2019-00899-1-1), Ministry of Science and Technology of the People's Republic of China (Grant No. 2017YFB1103000), National Natural Science Foundation of China (Grant No. 51375242), and Natural Science Foundation of Jiangsu Province (Grant No. BK20180483).

Competing Interests

The authors declare no competing financial interests.

Received: 2 November 2021 Revised: 21 October 2022 Accepted: 17 February 2023

Published online: 10 March 2023

References

- [1] T DebRoy, H L Wei, J S Zuback, et al. Additive manufacturing of metallic components - Process, structure and properties. *Progress in Materials Science*, 2018, 92: 112-224.
- [2] E Stepanova, N Pushilina, M Syrtanov, et al. Hydrogen effect on Ti-6.5Al-3.5Mo-1.5Zr-0.3Si parts produced by electron beam melting. *International Journal of Hydrogen Energy*, 2019, 44(55): 29380-29388.
- [3] Y Chen, C Yang, C Fan, et al. Grain refinement of additive manufactured Ti-6.5Al-3.5Mo-1.5Zr-0.3Si titanium alloy by the addition of La_2O_3 . *Materials Letters*, 2020, 275: 128170.
- [4] W T Yan, W J Ge, Y Qian, et al. Multi-physics modeling of single/multi-track defect mechanisms in electron beam selective melting. *Acta Materialia*, 2017, 134: 324-333.
- [5] A Aversa, M Moshiri, E Librera, et al. Single scan track analyses on aluminium based powders. *Journal of Materials Processing Technology*, 2018, 255: 17-25.
- [6] P Promopattum, R Srinivasan, S S Quek, et al. Quantification and prediction of lack-of-fusion porosity in the high porosity regime during laser powder bed fusion of Ti-6Al-4V. *Journal of Materials Processing Technology*, 2022, 300: 117426.
- [7] R Molaei, A Fatemi, N Sanaei, et al. Fatigue of additive manufactured Ti-6Al-4V, Part II: The relationship between microstructure, material cyclic properties, and component performance. *International Journal of Fatigue*, 2020, 132: 105363.
- [8] Y Liu, C Liu, W S Liu, et al. Optimization of parameters in laser powder deposition AlSi10Mg alloy using Taguchi method. *Optics and Laser Technology*, 2019, 111: 470-480.
- [9] S Sanchez, C J Hyde, I A Ashcroft, et al. Multi-laser scan strategies for enhancing creep performance in LPBF. *Additive Manufacturing*, 2021, 41: 101948.

- [10] H Gong, K Rafi, H Gu, et al. Analysis of defect generation in Ti-6Al-4V parts made using powder bed fusion additive manufacturing processes. *Additive Manufacturing*, 2014, 1-4: 87-98.
- [11] Z Wang, Z Y Xiao, Y Tse, et al. Optimization of processing parameters and establishment of a relationship between microstructure and mechanical properties of SLM titanium alloy. *Optics and Laser Technology*, 2019, 112: 159-167.
- [12] T Yang, T T Liu, W H Liao, et al. The influence of process parameters on vertical surface roughness of the AlSi10Mg parts fabricated by selective laser melting. *Journal of Materials Processing Technology*, 2019, 266: 26-36.
- [13] I Yadroitsev, P Krakhmalev, I Yadroitsava. Selective laser melting of Ti6Al4V alloy for biomedical applications: Temperature monitoring and microstructural evolution. *Journal of Alloys and Compounds*, 2014, 583: 404-409.
- [14] S Y Yamamoto, H S Azuma, S Suzuki, et al. Melting and solidification behavior of Ti-6Al-4V powder during selective laser melting. *The International Journal of Advanced Manufacturing Technology*, 2019, 103(9-12): 4433-4442.
- [15] T Furumoto, K Egashira, K Muneke, et al. Experimental investigation of melt pool behaviour during selective laser melting by high speed imaging. *Cirp Annals-Manufacturing Technology*, 2018, 67(1): 253-256.
- [16] M J Matthews, G Guss, S A Khairallah, et al. Denudation of metal powder layers in laser powder bed fusion processes. *Acta Materialia*, 2016, 114: 33-42.
- [17] P Bidare, I Bitharas, R M Ward, et al. Laser powder bed fusion at sub-atmospheric pressures. *International Journal of Machine Tools and Manufacture*, 2018, 130: 65-72.
- [18] S Y Pang, W D Chen, J X Zhou, et al. Self-consistent modeling of key-hole and weld pool dynamics in tandem dual beam laser welding of aluminum alloy. *Journal of Materials Processing Technology*, 2015, 217: 131-143.
- [19] H L Wei, Y Cao, W H Liao, et al. Mechanisms on inter-track void formation and phase transformation during laser powder bed fusion of Ti-6Al-4V. *Additive Manufacturing*, 2020, 34: 101221.
- [20] S A Khairallah, A T Anderson, A Rubenchik, et al. Laser powder-bed fusion additive manufacturing: Physics of complex melt flow and formation mechanisms of pores, spatter, and denudation zones. *Acta Materialia*, 2016, 108: 36-45.
- [21] T Zhang, H Li, S Liu, et al. Evolution of molten pool during selective laser melting of Ti-6Al-4V. *Journal of Physics D-Applied Physics*, 2019, 52(5): 055302.
- [22] C Tang, J L Tan, C H Wong. A numerical investigation on the physical mechanisms of single track defects in selective laser melting. *International Journal of Heat and Mass Transfer*, 2018, 126: 957-968.
- [23] Z Wang, W Yan, W K Liu, et al. Powder-scale multi-physics modeling of multi-layer multi-track selective laser melting with sharp interface capturing method. *Computational Mechanics*, 2018, 63(4): 649-661.
- [24] L Zhang, W H Liao, T T Liu, et al. In situ elimination of pores during laser powder bed fusion of Ti-6.5Al-3.5Mo-1.5Zr-0.3Si titanium alloy. *Acta Metallurgica Sinica (English Letters)*, 2021, 35(3): 439-452.
- [25] X Zhou, X H Liu, D D Zhang, et al. Balling phenomena in selective laser melted tungsten. *Journal of Materials Processing Technology*, 2015, 222: 33-42.
- [26] W H Yu, S L Sing, C K Chua, et al. Particle-reinforced metal matrix nanocomposites fabricated by selective laser melting: A state of the art review. *Progress in Materials Science*, 2019, 104: 330-379.
- [27] J Yin, D Wang, H Wei, et al. Dual-beam laser-matter interaction at overlap region during multi-laser powder bed fusion manufacturing. *Additive Manufacturing*, 2021, 46: 02178.
- [28] B Song, S Dong, H Liao, et al. Process parameter selection for selective laser melting of Ti6Al4V based on temperature distribution simulation and experimental sintering. *The International Journal of Advanced Manufacturing Technology*, 2011, 61(9-12): 967-974.
- [29] B U Scipioni, G Guss, S Wu, et al. In-situ characterization of laser-powder interaction and cooling rates through high-speed imaging of powder bed fusion additive manufacturing. *Materials & Design*, 2017, 135: 385-396.
- [30] J J Yang, J Han, H C Yu, et al. Role of molten pool mode on formability, microstructure and mechanical properties of selective laser melted Ti-6Al-4V alloy. *Materials & Design*, 2016, 110: 558-570.
- [31] P Bidare, I Bitharas, R M Ward, et al. Fluid and particle dynamics in laser powder bed fusion. *Acta Materialia*, 2018, 142: 107-120.
- [32] A F H Kaplan. Local absorptivity modulation of a 1 μ m-laser beam through surface waviness. *Applied Surface Science*, 2012, 258(24): 9732-9736.
- [33] M Ghayoor, K Lee, Y He, et al. Selective laser melting of 304L stainless steel: Role of volumetric energy density on the microstructure, texture and mechanical properties. *Additive Manufacturing*, 2020, 32: 101011.
- [34] A V Gusarov, I Yadroitsev, P Bertrand, et al. Heat transfer modelling and stability analysis of selective laser melting. *Applied Surface Science*, 2007, 254(4): 975-979.
- [35] S Y Liu, Y C Shin. Additive manufacturing of Ti6Al4V alloy: A review. *Materials & Design*, 2019, 164: 107552.
- [36] C C Zhang, H L Wei, T T Liu, et al. Influences of residual stress and micro-deformation on microstructures and mechanical properties for Ti-6.5Al-3.5Mo-1.5Zr-0.3Si alloy produced by laser powder bed fusion. *Journal of Materials Science & Technology*, 2021, 75: 174-183.

Submit your manuscript to a SpringerOpen[®] journal and benefit from:

- Convenient online submission
- Rigorous peer review
- Open access: articles freely available online
- High visibility within the field
- Retaining the copyright to your article

Submit your next manuscript at ► [springeropen.com](https://www.springeropen.com)